Steady-State and Transient Ultraviolet Resonance Raman Spectrometer for the 193–270 nm Spectral Region

SERGEI BYKOV, IGOR LEDNEV, ANATOLI IANOUL, ALEKSANDR MIKHONIN, CALUM MUNRO, and SANFORD A. ASHER*

Department of Chemistry, University of Pittsburgh, Pittsburgh, Pennsylvania 15260 (S.B., A.M., S.A.A.); Department of Chemistry, University at Albany, SUNY, Albany, New York 12222 (I.L.); Department of Chemistry, Carleton University, Ottawa, ON K1S 5B6 Canada (A.I.); and PPG Industries, Allison Park, Pennsylvania 15101 (C.M.)

We describe a state-of-the-art tunable ultraviolet (UV) Raman spectrometer for the 193–270 nm spectral region. This instrument allows for steady-state and transient UV Raman measurements. We utilize a 5 kHz Ti-sapphire continuously tunable laser (~20 ns pulse width) between 193 nm and 240 nm for steady-state measurements. For transient Raman measurements we utilize one Coherent Infinity YAG laser to generate nanosecond infrared (IR) pump laser pulses to generate a temperature jump (T-jump) and a second Coherent Infinity YAG laser that is frequency tripled and Raman shifted into the deep UV (204 nm) for transient UV Raman excitation. Numerous other UV excitation frequencies can be utilized for selective excitation of chromophoric groups for transient Raman measurements. We constructed a subtractive dispersion double monochromator to minimize stray light. We utilize a new charge-coupled device (CCD) camera that responds efficiently to UV light, as opposed to the previous CCD and photodiode detectors, which required intensifiers for detecting UV light. For the T-jump measurements we use a second camera to simultaneously acquire the Raman spectra of the water stretching bands (2500–4000 cm^{-1}) whose band-shape and frequency report the sample temperature.

Index Headings: **UV resonance Raman spectrometer; Biological macromolecules; Tunable UV laser; Nd:YAG laser; Subtractive double monochromator; Time-resolved measurements; Temperature jump; T-jump.**

INTRODUCTION

Raman spectroscopy is a routine technique in analytical chemistry, physical chemistry, materials science, and biological areas of research.[1–3] New inexpensive instruments have recently been commercialized for near-infrared (NIR) spectral region excitation by utilizing inexpensive diode lasers. This follows the development of Fourier transform infrared (FT-IR) Raman spectrometers that utilized 1.06 μm continuous wave (CW) Nd:YAG laser sources. Numerous applications using NIR excitation have been demonstrated over the last decade.[4–8] A major advantage of IR excitation, compared to the previously more common visible wavelength excitation, is that the IR laser excitation minimizes sample fluorescence.[9]

Excitation in the near infrared normally occurs far from any electronic transitions. In this case, the magnitudes of the Raman cross-sections are proportional to the square of the Raman polarizability, the derivative of the molecular polarizability for motion along the normal mode coordinate.[10] Most vibrations have similar Raman polarizabilities and thus give rise to similar intensities. Thus, all Raman allowed vibrations contribute similarly and complex samples give rise to congested complex spectra. The spectra are also weak and thus require relatively high sample concentrations.

The use of resonance excitation, where the excitation wavelength occurs within an electronic transition of the sample, can give rise to dramatic increases in the intensity of those vibrational normal modes whose nuclei are localized at the chromophoric segment.[10] The Raman intensity can increase by orders of magnitude (as high as ~10^8) for favorable cases. This leads to great selectivity and simple spectra that only display vibrations localized within the chromophore. Only molecules containing the resonant chromophore show resonance enhancement. This may be a particular analyte, or it may be a chromophoric segment of a macromolecule. For example, numerous studies of heme proteins and visual pigments utilized excitation in the visible spectral region to excite resonance Raman spectra of the heme and the polyene.[11–16]

More recently a number of groups have been working to extend Raman into the deep ultraviolet (UV) spectral region where all molecules show electronic transitions. Many of these groups are targeting UV resonance Raman excitation to excite within the UV chromophores of biological molecules, such as the aromatic amino acid ring $\pi \rightarrow \pi^*$ transitions[17–29] and the peptide bond $\pi \rightarrow \pi^*$ transitions.[30–33] In addition to the generally large resonance excitation enhancement, UV excitation has the further advantage that the light scattering efficiency scales with the fourth power of frequency; 200 nm excitation shows a 600-fold greater efficiency than would NIR excitation at 1000 μm. In addition, UV excitation avoids fluorescence interference; relaxed emission in condensed-phase samples does not occur below 250 nm with excitation below 250 nm.[34]

Received 24 June 2005; accepted 29 September 2005.
* Author to whom correspondence should be sent. E-mail: asher@pitt.edu.

0003-7028/05/5912-1541$2.00/0

We, as well as other groups, have been pioneering the development of UV Raman spectroscopy.[35–46] This work demonstrates that UV Raman secondary structure determination methodologies are the most sensitive methods for elucidating secondary structure of low concentrations of proteins in solution.[47] Moreover, this method can be used kinetically to investigate fast structural changes in proteins and peptides.[48–58] The methodology allows the convenient study of aromatic molecules at low concentrations. Species such as aromatic amino acids and nucleic acids are easily monitored and the spectra give information on hydrogen bonding and environment.[17–20,23–29,59]

The instrumentation for UV Raman studies has rapidly evolved over time. The earliest pre-laser instruments utilized mercury arc excitation.[60,61] The first modern instruments built in the mid-1980s utilized low duty cycle Nd:YAG lasers that were frequency tripled, quadrupled, and Raman shifted, and/or utilized frequency doubled Nd:YAG to excite a dye laser that was frequency doubled and/or mixed with the 1.06 μm fundamental to achieve tunable excitation down to 212 nm.[35,36] These laser sources caused nonlinear photochemistry and depletion of the ground-state populations of samples that led to Raman saturation phenomena.[62] These were useful phenomena for excited-state studies but were a nuisance in measurements that attempted to measure ground-state resonance Raman spectra.

More recent spectrometers utilized high repetition rate (300 Hz, 20 ns pulse width) XeCl excimer lasers to pump dye lasers, which were frequency doubled down to 206 nm excitation. These higher duty cycle lasers helped to avoid nonlinear phenomena.[63,64] Unfortunately, UV Raman measurements using these lasers were labor intensive due to the low stability of the laser dyes and the gallons of dye solutions required.

Dramatic improvements in laser excitation sources occurred with the development of intracavity doubled argon and krypton-ion lasers using β-barium borate (BBO) nonlinear crystals. This allowed the generation of CW radiation with wavelengths of 206.5 and 234 nm for krypton[65] and 228.9, 238, 244, 248, and 257 nm for argon-ion lasers.[38] Such excitation sources were reliable, with low peak powers that eliminated nonlinear, saturation, and thermal degradation problems. The main disadvantage of these lasers was that they only offered a limited number of wavelengths.

In the work here we describe a state-of-the-art UV Raman spectrometer that for steady-state measurements utilizes a continuously tunable laser source between 193 and 240 nm that is based on a Ti:Sapphire laser. This quasi-continuous wave 5 kHz laser has a ~20 ns pulse width that for many samples avoids nonlinear phenomena. It should be noted that our Ti:Sapphire laser source is somewhat similar to the Ti:Sapphire UV laser recently reported by the Spiro group.[66]

Our UV Raman spectrometer is also designed for kinetic measurements (nanoseconds to milliseconds) by utilizing two high repetition rate Nd:YAG lasers. One laser generates nanosecond pump pulses in the IR, visible, or UV spectral region, while the other generates the nanosecond UV probe pulses to excite the UV Raman spectra at the appropriate delay time.[52]

EXPERIMENTAL

Samples. Penta-alanine $(Ala)_5$, acetonitrile, and sodium perchloride were purchased from Sigma Aldrich (St. Louis, MO) and were used as received. Sodium perchlorate is used as an internal standard. Munsell color white reflectance standard, which is a highly purified powder of barium sulfate, was purchased from GretagMacbeth LLC (New Windsor, NY).

Horse heart metmyoglobin (holo-Mb) was purchased from Sigma Chemical (St. Louis, MO). The heme group was removed by 2-butanone extraction as described by Teale.[67] The apomyoglobin (apo-Mb) was then purified by Sephedax-25 gel chromatography, lyophilized, and stored at −20 °C. We used about 40 μM solutions for steady-state and kinetic Raman measurements in D_2O. We use D_2O rather than H_2O due to a lower deuterium oxide extinction coefficient at 1.9 μm. This allowed us to use less concentrated protein solutions. Concentrations were determined from the absorption spectra by using a Perkin-Elmer Lambda 9 UV-VIS absorption spectrometer. We used a molar absorption coefficient value of 14 260 M^{-1} cm^{-1} at 280 nm.

Spectrometer Efficiency Measurements. The spectrometer throughput efficiency was measured by recording the transmittance of UV light from a standard ultraviolet spectral irradiance deuterium lamp (UV-40) manufactured by Optronic Laboratories Inc (Orlando, FL). The light from this lamp was scattered from the surface of the barium sulfate powder pressed into a holder, which was used as a Lambert surface. $BaSO_4$ works well as a reflectance standard in the UV because of its high stability and low absorbance.[68–70] The ~5 mm thick pressed $BaSO_4$ powder scattered all of the incident light. It was placed in the normal sample position. The normal to the $BaSO_4$ reflectance surface was oriented to lie along the spectrometer optic axis. The standard intensity lamp illuminated the barium sulfate surface at an angle of ~45° to this normal.

INSTRUMENTATION

Continuously Tunable Ultraviolet Laser. To cover the 193–240 nm spectral region we use two different Positive Light Co. (Los Gatos, CA) Indigo-S tunable UV laser systems. These two systems contain Evolution-15 pump lasers, tunable Ti:Sapphire oscillators, and the appropriate nonlinear crystals and optics to generate the fourth harmonic of the Ti:Sapphire output. One system uses two successive frequency doublers to generate tunable light from 210 to 240 nm. Because crystals are not available to frequency double below 206 nm, we obtain shorter wavelengths by mixing the third harmonic with the fundamental to generate continuously tunable fourth harmonic UV radiation between 193 and 210 nm. Longer wavelengths from 240 to 270 nm are also available as the output of the third-harmonic generator.

The Ti:Sapphire oscillator layouts for generating the fundamental or for generating the frequency doubled output are shown in Figs. 1A and 1C. The optical diagram of the nonlinear optics for converting the fundamental to the third harmonic and for mixing with the fundamental is shown in Fig. 1B. Figure 1D shows the optical diagram for the frequency doubled system.

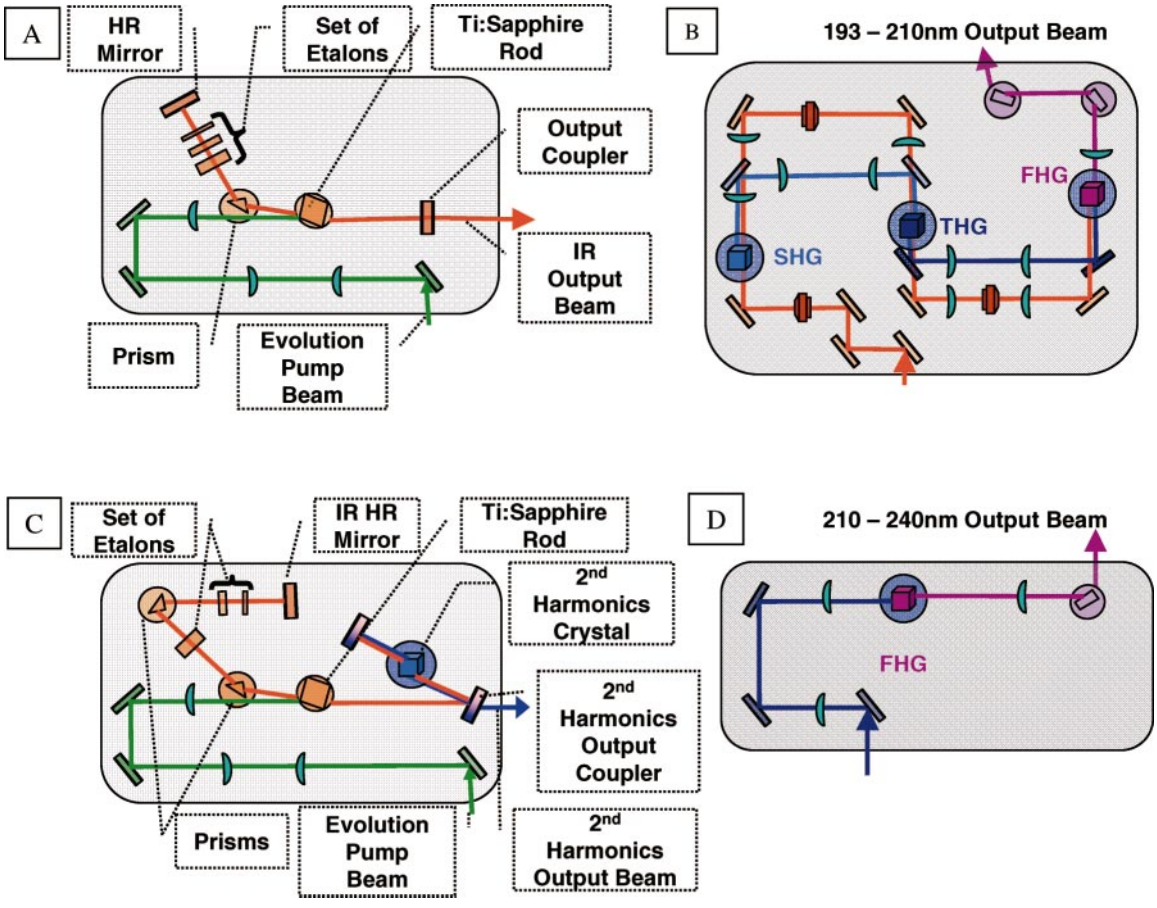

FIG. 1. Optical layouts for (**A**) fundamental Ti:Sapphire output and (**C**) intra-cavity doubled Ti:Sapphire oscillators. Optical configuration for (**B**) the 193–210 nm frequency doubling and mixing package, and (**D**) the 210–240 nm frequency doubling.

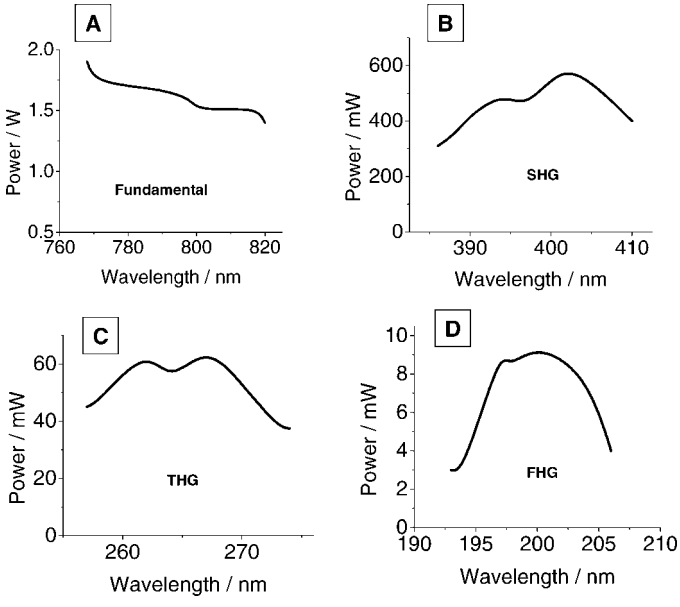

FIG. 2. Typical output average powers for the 193–210 nm Indigo-S DUV tunable laser. (**A**) Oscillator IR power, (**B**) second harmonic, (**C**) third harmonic, and (**D**) fourth harmonic.

The Evolution-15 pump laser is an acousto-optically Q-switched Nd:YLF system operating at 5 kHz frequency to generate a 1053 nm wavelength fundamental with a 100 to 350 ns pulse duration depending on the pulse energy. This laser is intra-cavity frequency doubled using a lithium tri-borate (LBO) crystal that is noncritically† phase matched by heating to ~320 °F to generate 527 nm light that is used to pump the Ti:Sapphire oscillator. The wavelength tunable Ti:Sapphire oscillator utilizes etalons to generate narrow-linewidth NIR radiation, which is converted to UV radiation by the nonlinear optics harmonics packages.

The 193–210 nm laser harmonics package consists of a second-harmonic generator (SHG) that converts the 772–820 nm Ti:Sapphire IR fundamental to 386–410 nm light with ~20% efficiency. The THG crystals mix the 386–410 nm light with the IR fundamental to produce the 257–273 nm third harmonic with an efficiency of up to 10%. The final stage mixes the third harmonic with the residual fundamental to produce 193–210 nm light with a somewhat lower efficiency of about 5%. The deep UV output power depends on the wavelength and varies from ~9 mW at ~200 nm to ~3 mW at the edges of the 193–210 nm spectral region. Typical output powers for the 193 nm system are shown in Fig. 2.

† Birefringence of the BBO crystal can be adjusted by using its temperature dependence. This is called noncritical phase matching or temperature phase matching.

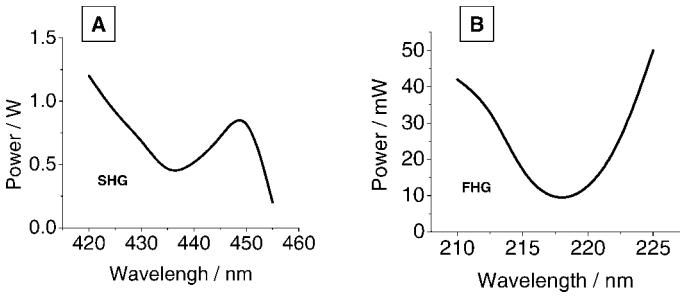

FIG. 3. Typical output powers for 210–240 nm Indigo-S DUV tunable laser. (**A**) Intracavity doubled oscillator SHG power. (**B**) Fourth harmonic UV power.

In the 210–240 nm system IR light generated by the Ti:Sapphire oscillator is intracavity frequency doubled. This second harmonic light (420–480 nm) is directly converted to the UV by further frequency doubling. The overall efficiency is ~20%, which results in 10–40 mW of 210 nm to 240 nm UV radiation. Typical output powers are shown in Fig. 3.

Pulsed Infrared, Visible, and Ultraviolet Laser. The transient Raman instrument utilizes two Coherent Inc. (Santa Clara, CA) Infinity Nd:YAG lasers (Fig. 4). These lasers have the exceptionally high quality temporal and spatial beam profiles essential for efficient frequency conversion by Raman shifting multiple harmonics in hydrogen or other gases.[35,71–73] The Infinity Nd:YAG laser consists of an internal diode pump and Q-switched master oscillator, which provides the initiating pulse for the dual rod, single lamp amplifier stage. This laser is equipped with a feedback system. A phase conjugate mirror (SBS cell) is utilized to correct for wave front distortions created by the thermal and stress induced effects in the Nd:YAG rods. As a result, the Infinity system can produce superior quality laser pulses independently of repetition rate and output power. We also recently acquired an XPO optical parametric oscillator system to continuously change the wavelength of the heating IR pulse.

The layout of the temperature jump (T-jump) instrument is shown in Fig. 5. Our transient Raman spectrometer consists of two electronically synchronized Coherent Nd:YAG Infinity lasers. The first laser generates an IR heating pulse or a visible or UV pulse to excite the system. The other Coherent Nd:YAG Infinity laser generates a delayed UV pulse to excite the resonance Raman scattering. The lasers operate at 100 Hz and generate 3.5 ns UV pulses.

In the original design[52] the heating beam was obtained by Raman shifting the YAG fundamental in H_2 to 1.9 μm (first Stokes) as described in earlier publications.[74] The Nd:YAG fundamental is focused by lens *L3* into the Raman shifter *RS#2* filled with H_2 at a high pressure of ~1000 psi. The first Stokes beam at 1.9 μm is separated by a Pellin–Broca prism and directed to the sample by a few gold-coated mirrors.

This setup allows us to generate a T-jump as high as 65 °C when the 1.5 mJ, 1.9 μm laser pulses are focused to a ~200–300 μm diameter spot in the flow-stream.[51] However, this very high water absorbance of ~40/cm at 1.9 μm requires us to use highly concentrated protein/peptide solutions. This is because our experiment requires us to collect Raman scattering from the same sample depth that we heat; the UV Raman exciting light must experience similar sample absorbance as the IR T-jump pulse. Since we use a recirculating sample stream that generally utilizes ~10 mL of solution, we require large amounts of sample, which can be very expensive. In addition, high concentrations are often undesirable because many biological macromolecules aggregate at high concentrations.

We have partially solved this problem by using a Coherent Infinity-XPO tunable optical parametric oscillator (OPO). This allows for IR tuning from ~1 μm to ~2.2

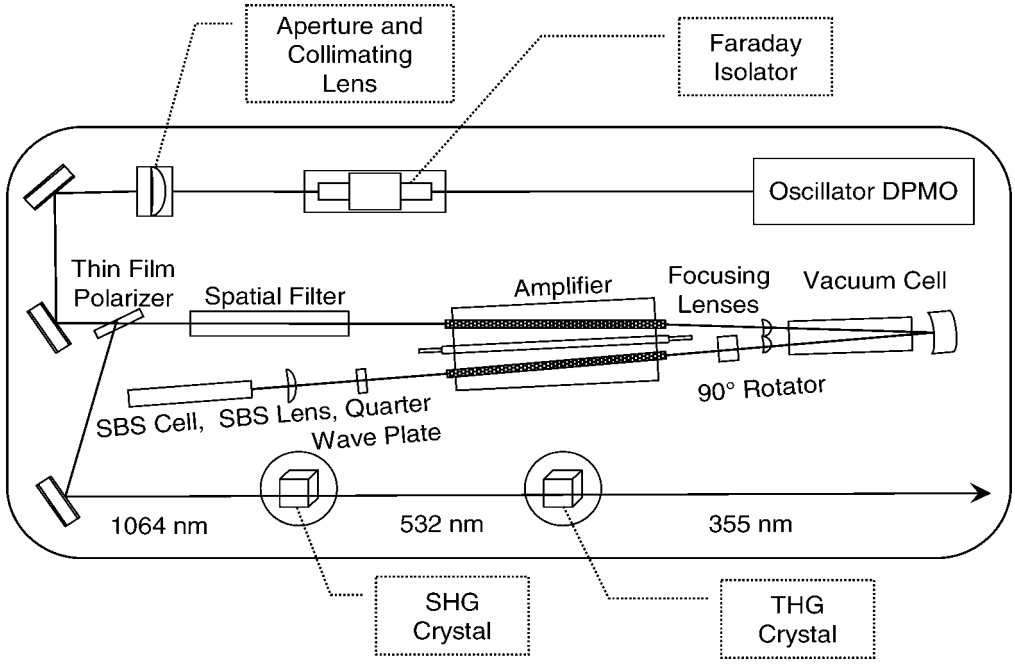

FIG. 4. Optical layout of the Coherent Infinity Nd:YAG laser with second and third harmonic crystals.

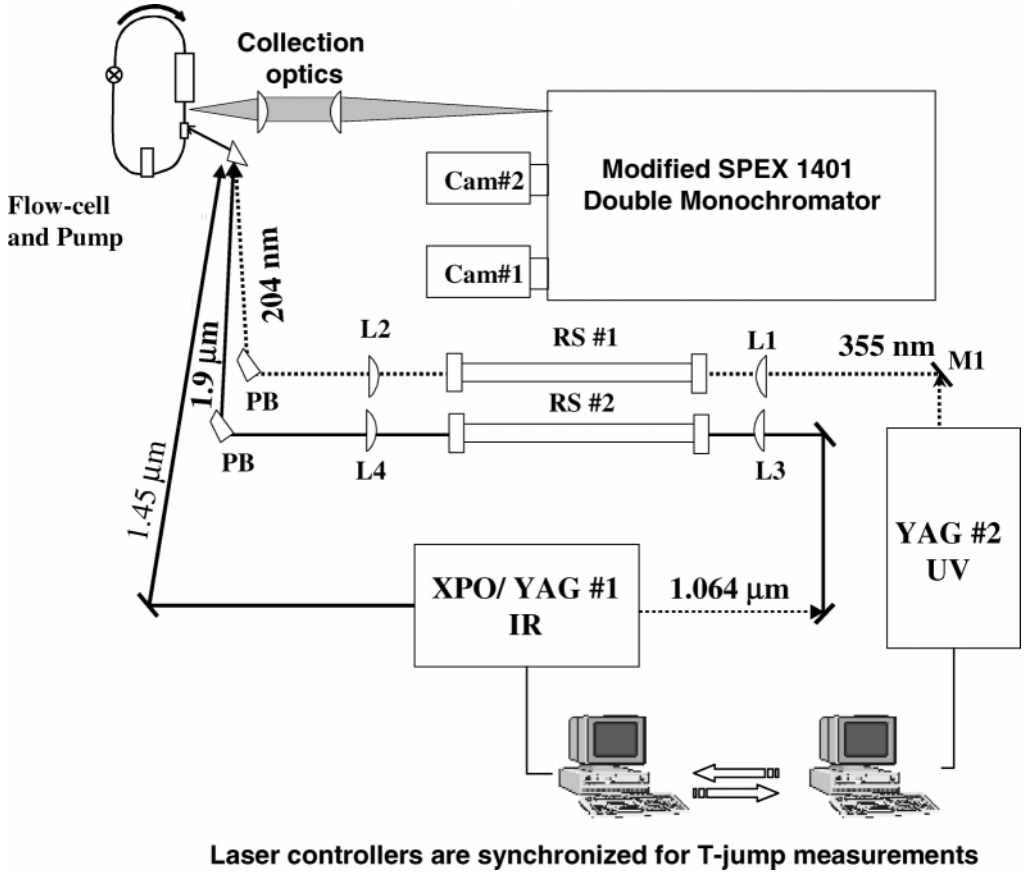

FIG. 5. Schematic diagram of the spectrometer for UV resonance Raman transient (T-jump) measurements.

μm. Our desired wavelength is 1.45 μm, where the water absorption is reduced to ~12/cm, which allows us to decrease the peptide/protein concentration. The main disadvantage of this approach is a lower T-jump due to lower IR absorption. Further, the Infinity XPO laser is less efficient than the Stokes Raman scattering process that generates 1.9 μm light.

The laser used to generate 204 nm radiation (YAG #2) is frequency tripled. Approximately 3 W of this 355 nm UV radiation is directed onto the dichroic mirror *M1*, which filters out most of the second harmonic. This light is then focused by lens *L1* into the Raman shifter *RS #1*, which is filled with 60 psi hydrogen (Fig. 5). The resulting polychromic radiation is focused by lens *L2* onto a Pellin–Broca prism, which disperses the light and separates out the 204 nm fifth anti-Stokes beam. This light (~3 mW) is focused into the volume element of the sample heated by the IR pulse in order to excite the UV resonance Raman spectra. The delay time between heating and probing pulses can be varied between ~5 ns and 6 ms with ~0.5 ns accuracy in the nanosecond and microsecond regions and with ~100 ns accuracy in the millisecond region.

Multichannel Detectors. As discussed for transient Raman measurements, we separately and simultaneously measure the high frequency (2500 to 4000 cm^{-1}) and low frequency (800 to 1800 cm^{-1}) Raman spectra by optically selecting the high frequency portion of the Raman scattering in the first stage of the monochromator. Thus, we use two separate multichannel detectors.

We utilize a liquid nitrogen cooled Princeton Instruments Spec-10:400B digital charge-coupled device (CCD) detector as the high signal-to-noise (S/N) detector for accumulation of highly resolved spectra in the 800–1800 cm^{-1} region. It has a 1340 × 400 array of 20 × 20 μm pixels (26.8 mm × 8.0 mm image area). It is a cryogenically cooled back-thinned CCD with a reported >30% quantum efficiency in the deep UV region.

We have utilized ever-improving detectors over the years as we have refined our Raman instrument. It turns out that we could only determine the utility of a detector by actually testing it in our laboratory side by side with detectors that we were already successfully using. Manufacturers' spectral efficiency specifications were repeatedly found to be completely unreliable.

The present camera is the first CCD that we found capable of detecting UV light with significant efficiency. This CCD camera gives us ~3-fold better spectral S/N than did our Princeton Instruments solar blind intensified CCD ICCD-Max-1024-E, which in turn, had ~3-fold better S/N than the non-solar blind intensified Princeton Instruments detector, ICCD 1024 MS-E, that we previously utilized, which had a ~10-fold improved S/N compared to our earliest EG&G Princeton Applied Research 1420 and 1456 intensified photodiode arrays.

Over the last decade we have tested multiple back-thinned CCD cameras from numerous manufacturers in our laboratory that we found were unable to detect UV photons in spite of their quoted high UV quantum yields. The manufacturers were quite confused by these results.

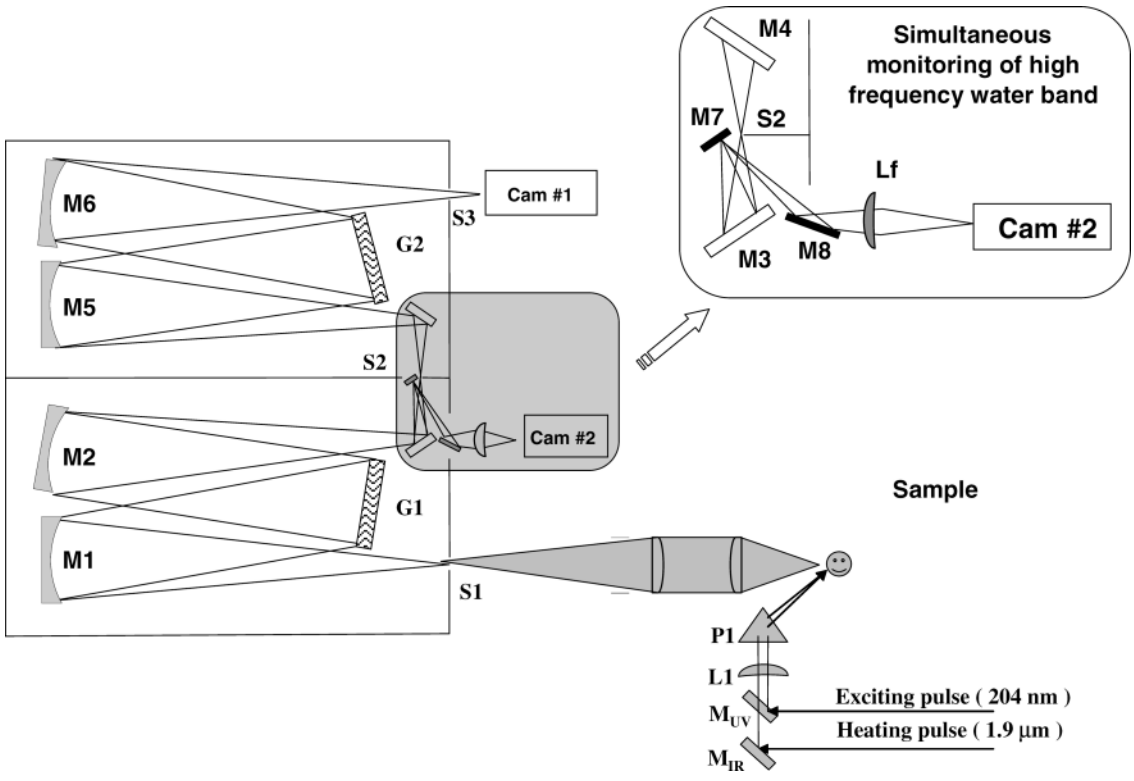

FIG. 6. Modified SPEX 1401 double monochromator and collection optics. The insert shows the optics used to direct the ~2500–3500 cm^{-1} Raman scattered light dispersed by grating G1 to a second detector (Cam #2).

Ultraviolet Raman Spectrograph. The scattered light was dispersed by a SPEX 1401 0.75 m Czerny–Turner (originally additive) double monochromator, $f/6.8$ (Fig. 6). Spectrometer stray light is the major interference that limits the Raman spectral S/N ratios. This stray light results from the lack of complete rejection of the Rayleigh scattering. Some fraction of light at this wavelength finds itself in the spectrograph image plane situated on the detector overlapping the actual Raman inelastically scattered light. Thus, it is detected as if it were Raman scattered light. This light, which underlies the Raman spectrum, is known as instrumental stray light.[75,76] It originates from blemishes in dispersive and reflective elements of the monochromator, dust particles, etc., and from unintentional light reflections and scattering that can derive, for example, from retro-diffraction from the CCD detector or from the pincushion intensifier.[77] This stray light can introduce artifacts and can decrease the Raman spectral S/N. It can also contribute features that interfere and in the worst cases can confound the Raman spectral measurements. Good monochromator design attempts to substantially reduce unwanted reflections and scattering.

We significantly modified the spectrometer to minimize the stray light, to optimize its efficiency for deep UV measurements, and to permit simultaneous monitoring of the high frequency and mid frequency Raman spectra at high resolution. We minimized stray light by using the double monochromator in partial subtractive dispersion. Subtractive dispersion double monochromators were originally described by van Cittert[78] as well as others.[79–83] In contrast to the additive configuration, when both gratings of the monochromator disperse light in the same direction, subtractive dispersion uses the second grating to partially or completely undisperse the light.

This is a method often used in triple monochromators, where the first stage disperses the spectrum, and the edge of a slit blocks the Rayleigh scattering. This dispersed light, without the Rayleigh scattering, is then sent to a second completely subtractive stage that recombines the light onto the entrance slit of a spectrograph. This ''pink light'' is then dispersed by the spectrograph stage onto a multichannel detector, where the stray light is significantly reduced.

We wish to optimize the throughput efficiency of the spectrometer and, thus, only utilize two stages by using a double monochromator in subtractive dispersion in a manner similar to that reported by Mathies.[84] The originally linked gratings of our vintage 1960 SPEX 1401 double monochromator *G1* and *G2* were decoupled by removing the mechanical connection. Both gratings were then controlled by two separate micrometer screw drives threaded through holes in the faceplate of the spectrometer. This allowed us to use these gratings in a subtractive dispersion configuration. As discussed below, this significantly reduces the stray light occurring at the Rayleigh frequency.

Figure 7 compares the performances of double spectrometers that operate in additive and subtractive dispersion. In both cases the first stage utilizes a 600 grooves/mm grating in the +1 order. In order to achieve identical linear dispersions at the final second stage image plane, the second stage additive dispersion utilizes a 2400 grooves/mm grating used in the $+1^{st}$ order (case I). For

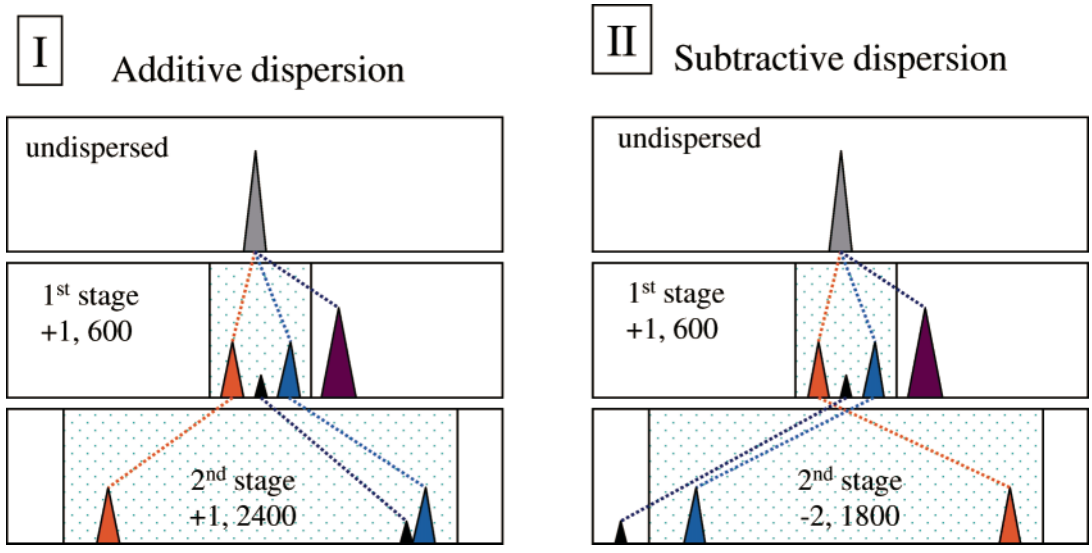

FIG. 7. Reduction of stray light by the use of (**II**) subtractive rather than (**I**) additive dispersion. Raman spectral intensities are shown at the spectrograph image planes after the first and second spectrograph stages. A small black peak represents a portion of a stray light at the excitation frequency but situated at the center of the detector, and the large purple peak is the Rayleigh line, while the red and blue peaks are the low frequency and the high frequency Raman bands, respectively.

subtractive dispersion we use a second stage 1800 grooves/mm grating in the -2^{nd} order (case II).

The first stage disperses both the Rayleigh light (purple triangle) and the Raman spectrum. The red and blue triangles indicate Raman bands at the extreme edges of the measured Raman spectra. The small black triangle indicates a spatially defined portion of the stray light at the Rayleigh wavelength, which is localized on the image plane at an artifactual location at an apparent intermediate Raman wavelength. In additive dispersion, the second monochromator increases the linear dispersion to increase the distance between the ''red'' and ''blue'' bands. The Rayleigh stray light band is also further dispersed, but given the desired linear dispersion, remains within the Raman spectral interval in the image plane. The Raman lines are equivalently dispersed as if a single 3000 grooves/mm grating had dispersed the light. The stray light was dispersed by only the second stage and was dispersed by a single 2400 grooves/mm grating. Thus, the stray light remains in the Raman spectral region but is blue shifted by the dispersion in the second stage to the high frequency side of the spectrum (to the low frequency spectral portion).

In subtractive dispersion (II), our second grating has six times the dispersion of the first grating. Thus, after the second stage the light ends up with four times the dispersion of the first stage. However, the spectrum is spatially dispersed backwards, with the red band on the left and the blue on the right compared to additive dispersion. The stray light is dispersed far towards the blue (the low frequency portion of the Raman spectrum). There is more dispersion to reject the stray light in the subtractive dispersion situation. The Raman light is dispersed by the equivalent of a single 3000 grooves/mm grating, the same as in additive dispersion. In contrast, the stray light is dispersed by the equivalent of a 3600 grooves/mm grating.

To increase the spectrometer efficiency, all of the original evaporated aluminum mirrors in the spectrometer (*M1–M6*) were dielectrically coated by CVI Laser LLC (Albuquerque, NM) to give a ~95% reflectance efficiency for the 200–215 nm and 229–244 nm spectral regions. This contrasts with a ~90% reflectance for the MgF_2 coated UV enhanced Al mirrors, which degrades over a year to only a 70% reflectance. This increased reflection efficiency has a significant impact since the double monochromator has a minimum of six mirrors. For convenience we utilize the monochromator backwards by placing the entrance slit on the exit image plane and by placing the detector at the normal entrance slit plane.

The total throughput of the spectrometer is shown in Fig. 8. The spectrometer efficiency varies between 15 and 20% in the 200–230 nm spectral region. The spectrometer efficiency drops rapidly for wavelengths shorter then 195 nm, becoming zero at ~191 nm. We are unsure of the phenomenon that limits the efficiency at the shortest wavelengths since we do not have reliable data on the barium sulfate powder reflectance or on the CCD camera quantum efficiency below 200 nm. In addition, our spectrometer efficiency was measured in air, which can strongly absorb UV radiation at wavelengths shorter than 200 nm. The throughput profile below 200 nm shows a series of narrow troughs due to the well known Schumann–Runge molecular oxygen absorption bands.[85] These bands also show up in the UVRR spectra (see below).

A small plane mirror *M7* was attached onto the edge of the middle slit *S2* in order to deflect the high frequency part of the Raman spectrum to mirror *M8*, which focuses it onto a second camera attached to the first stage of the monochromator. We utilized an EG&G Princeton Applied Research 1456 intensified photo diode array with 1024 25 μm × 2.5 mm active elements (Fig. 6). The second detector detects the ~2500 cm^{-1} to ~4000 cm^{-1} Raman spectral region, which for aqueous solutions is dominated by the water OH stretching band, which changes band shape with the solution temperature.[86]

This detector has a S/N approximately 90-fold below

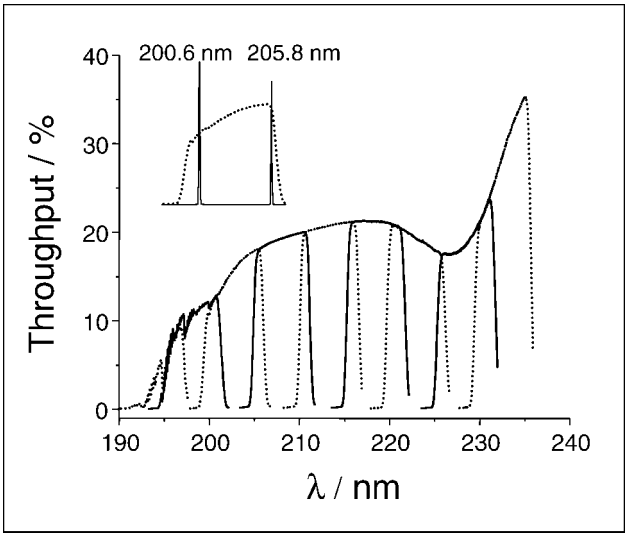

FIG. 8. Spectrometer efficiency (collection optics, monochromator, and detector) for the 193–235 nm region. The total curve is composed of nine separately measured ~6 nm segments at different grating positions. Each segment was wavelength calibrated by using the output of the Indigo-S tunable DUV lasers described above. The inset shows how the separate segments were wavelength calibrated by using the Rayleigh light scattered by the barium sulfate powder Lambert surface. The total throughput was normalized to the standard D_2-lamp irradiance. The absolute throughput of the standard lamp was determined by measuring the transmission of a 220 nm laser beam through the spectrometer.

that of the CCD camera. However, the intensity of the Raman water stretching band is very high and the S/N of the high frequency spectra are sufficiently high to accurately determine the T-jump temperature.

Spectral Resolution. The spectral resolution (SR) is usually defined as the minimum frequency separation between two peaks in the spectra that the instrument can resolve. SR is mainly determined by the resolving power of a monochromator given the size of a single light-sensitive element (here a CCD pixel) in the detector system. For two peaks to be resolved at the CCD detector, their maxima should be separated by at least one pixel with a decreased intensity between them. In the best case, two resolved peaks at the CCD sensor would span 3 pixels.

The reciprocal linear dispersion, R_d of the SPEX 1401 monochromator can be written as in Eq. 1 by considering a single stage Czerny–Turner spectrograph with an equivalent grating:‡

$$R_d = d\frac{\cos\beta}{f|m|} \quad (1)$$

where d is the distance between grooves of the equivalent grating, β is the angle between the grating normal and diffracted ray for an equivalent single monochromator, f is the focal length of the last mirror focusing the spectrum on the CCD detector, and m is the order of diffraction of the equivalent grating. At λ_{exc} = 204 nm, and R_d = ~0.32 nm/mm or ~75 cm^{-1}/mm. The limiting spectral resolution, SR_{lim} of our spectrograph consisting of a SPEX 1401 monochromator and Spec-10:400B digital camera can be calculated using Eq. 2:

‡ In our case equivalent grating has a groove density of (1800 × 2) − 600 = 3000 grooves/mm.

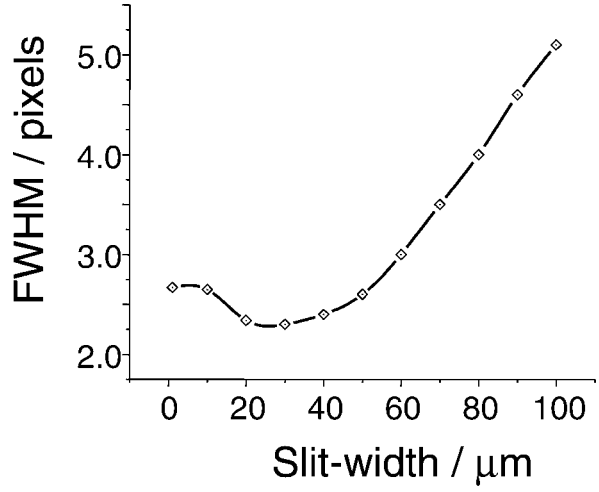

FIG. 9. Dependence of width (FWHM) of the low pressure atomic Hg lamp line at (265.204 nm) upon slit width of the SPEX 1401 monochromator.

$$SR_{lim} = R_d(cm^{-1}/mm) \times P_w(mm/pix) \times 3\ (pix) \quad (2)$$

where R_d is a reciprocal linear dispersion of the monochromator, P_w is the detector pixel width, and 3 is a minimum number of pixels to record two resolved bands. The pixel width of the Spec-10:400B digital camera is 20 μm, giving us a limiting spectral resolution of ~4.5 cm^{-1}.

Figure 9 shows the experimentally determined dependence of the full-width at half-maximum (FWHM) of a mercury atomic emission line upon the spectrometer entrance slit width. Atomic emission bands of low pressure lamps have <1 cm^{-1} linewidths. Thus, our observed linewidth is limited by our spectrograph resolution. A 100 micrometers slit projected onto the CCD imaging plane covers ~5.1 pixels, which is close to the value expected, given our Spec-10:400B CCD camera pixel size of 20 micrometers. At a ~204 nm excitation wavelength and 100 micrometers slit width, the FWHM of the Stokes Raman band in the protein amide region (~800–1800 cm^{-1}) would be 5 pixels × 1.5 cm^{-1}/pixel = 7.5 cm^{-1}.

The width of the mercury line decreases with decreasing slit width down to ~50 micrometers, after which the slope flattens, reaching its minimum of ~2 pixels or ~3 cm^{-1} at a monochromator slit width of ~20 micrometers. The increase in linewidth at small slit widths presumably is due to diffraction at the slit aperture.

The resolution of the spectra accumulated by the second camera is significantly lower because light is dispersed only by the first, low groove density grating in the first stage. R_d calculated from experimental data at λ_{exc} = 204 nm is ~400 cm^{-1}/mm in the water stretch region, which gives us the limiting spectral resolution of ~30 cm^{-1}. However, this resolution is adequate for the broad OH stretching bands of liquid water as shown by Fig. 10A, which shows the Raman spectra of acetonitrile and water. The water band at ~3200 cm^{-1} is due to OH stretching while the acetonitrile bands at ~2943 cm^{-1} and ~2253 cm^{-1} derive from CH and CN stretching, respectively.

Figure 10B shows two water spectra measured by the second detector at two different temperatures (70 °C and 0 °C) and the difference between them. The OH stretch-

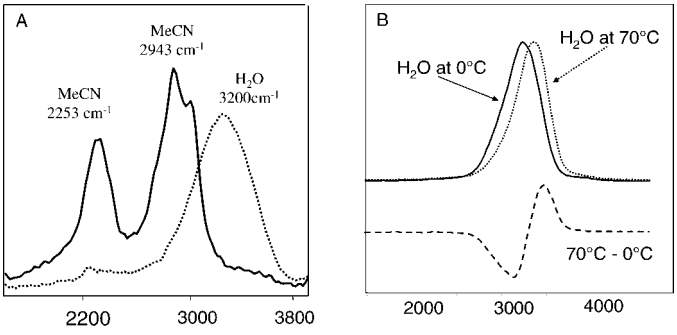

FIG. 10. (**A**) UVRR spectra of acetonitrile and water excited at 204 nm detected by the second EG&G 1456 Princeton Applied Research Intensified Diode Array detector. (**B**) Water OH stretching band temperature dependence at 0 and 70 °C.

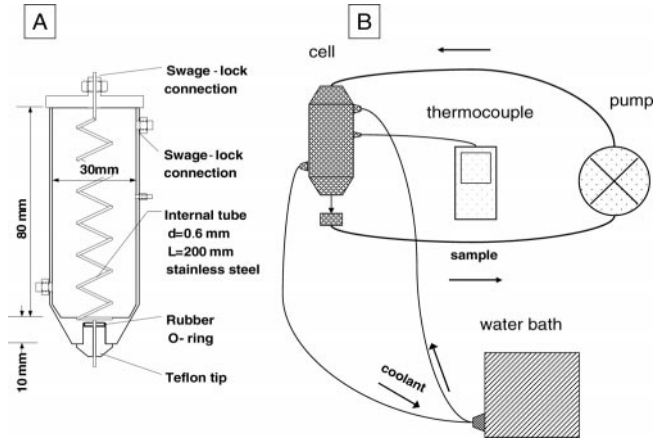

FIG. 11. (**A**) Temperature controlled flow-cell used for liquid samples. The sample cell was constructed from stainless steel and brass. A glass cell was used for samples sensitive to metal ions. The 0.6 mm diameter internal tube is ~200 mm long to allow efficient heat exchange with the thermally controlled reservoir. (**B**) Temperature controlled flow system connections. The Micropump Inc model 120 pump obtained from Cole-Parmer Instrument Co. (Vernon Hills, IL) was controlled by a Model 75225 Pump Drive Controller, which circulates the sample at a ~0.15–1.5 mL/s flow rate. The flow rate is adjusted to minimize stream instabilities to avoid laser reflections and light scattering. This is especially important for the time-resolved T-jump measurements, where heating and probing pulses must be precisely superimposed on the stream surface. This system requires 10 mL of solution for normal operation. The temperature of the sample solution is controlled by a circulating thermostated water–thylene glycol solution whose temperature is controlled by a thermostated water bath.

ing band shows the shift to higher frequency, which is associated with hydrogen bonding strength decrease as the temperature increases. This is a complex band, which can be fitted with four Gaussian components. Each component is assigned to water molecules in different hydrogen bonding states.[87] Much of the overall band shape change occurs due to redistribution of the water molecules among those states as the temperature changes. The measured value of $\Delta I/I_0$ can be used to calculate the solution temperature change.[51] Thus, we use these Raman spectra as an internal thermometer for determining the temperature of the small spot (~200 μm in diameter) heated by the IR pulse during the T-jump experiment.

Sample Handling. Ultraviolet Raman measurements require constant exchange of the illuminated sample volume during the experiment. This is especially important if pulsed lasers with high peak powers are used for Raman excitation. These pulsed sources may cause sample heating and photochemical degradation. For liquid samples our temperature controlled open stream system produces the highest signal-to-noise ratios (Fig. 11). However, this sample cell requires a relatively large sample volume (~10 mL) and cannot be used with highly volatile liquids.

We use a thin quartz capillary for smaller 50 μL volumes of solution.[88] Temperature controlled quartz cells[19] with a magnetic stirrer are utilized when the sample may not be exposed to the air. Other types of quartz cells are commercially available from manufacturers such as Starna Cells Inc. (Atascadero, CA) or Uvonic Instruments Inc. (Plainview, NY). We also utilize rotating quartz nuclear magnetic resonance (NMR) tubes to contain sample solutions for backscattering Raman measurements. The main disadvantage of quartz cells is the interference of SiO_2 Raman bands. The data reported here utilized the open stream system.

Dielectric coated mirrors and fused silica prisms are used to direct the laser beam onto the sample. The backscattered Raman light is collected and focused onto the spectrometer slit using a 50 mm diameter fused silica plano-convex lens matched to the spectrometer *f*/number. We have used the transient T-jump spectrometer to examine the earliest events in protein folding.[51,52]

Steady-State and Transient Measurements. Figure 12 shows UVR Raman spectra of penta-alanine (Ala_5) in water solution taken with 193 and 204 nm excitation. Both excitation wavelengths are within the $\pi \rightarrow \pi^*$ transition of the peptide bond,[89] which results in selective enhancement of the amide Raman bands. Since the Raman amide band frequencies and cross-sections are sensitive to backbone geometry[81,90,91] they provide direct quantitative information about peptide/protein secondary structure.[30,47,92,93] Penta-alanine in water shows the typical UV resonance Raman spectra of a polypeptide chain in a PPII conformation[90] ($\psi \approx 145°$, $\varphi \approx -75°$) with the amide I band at ~1663 cm^{-1}, the amide II band at ~1560 cm^{-1}, the amide III band at ~1254 cm^{-1}, and $C_\alpha H$ bending bands at ~1371 cm^{-1} and at ~1401 cm^{-1}. The sharp

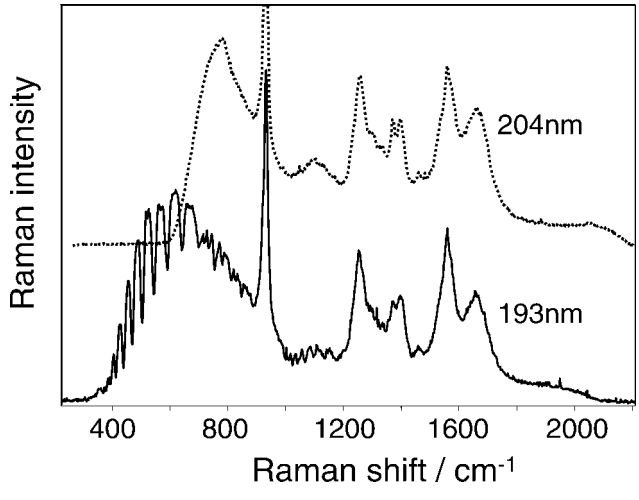

FIG. 12. UVRR spectra of $(Ala)_5$ in water (C = 0.2 mg/mL) at room temperature. Accumulation time for each spectrum is 5 min with a slit width of 100 μm.

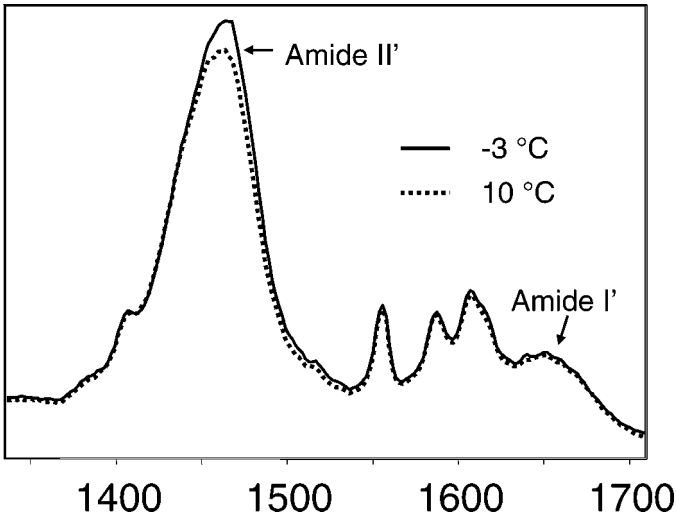

FIG. 13. Steady-state UVRR spectra of apo-Mb at −3 amd +10 °C in D_2O, pD ~ 6, concentration is 40 μM. The amide II' intensity decrease indicates apo-Mb refolding.

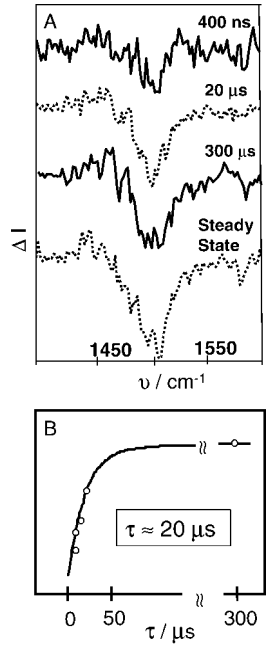

FIG. 14. (**A**) Apo-Mb difference spectra obtained by subtracting steady-state spectra at −3 °C from transient spectra measured at time delays of 400 ns, 20 μs, 300 μs, and at an infinite time delay (steady state). (**B**) Relaxation curve for apo-Mb refolding after T-jump from −3 to 10 °C. Refolding is monitored by a change in the amide II' intensity. The data is best fit by single exponential decay with a relaxation time of ~20 μs.

and intense band at ~932 cm^{-1} is due to ClO_4^- that we use as an internal standard.

The broad and intense band at low frequencies is mainly due to H_2O bending with some contribution from stray light. In the spectrum excited with ~193 nm light, a series of narrow troughs appears on the broad OH bending band of water at frequencies below 700 cm^{-1} that are due to molecular oxygen absorption by the Schumann–Runge bands of O_2, which arise from the transition $B^3\Sigma_u^- \leftarrow X^3\Sigma_g^-$ in the 175–205 nm region.[85] The UV light oxygen absorption does not significantly affect the 193 nm higher frequency amide region, but shorter excitation wavelengths would require an oxygen-free atmosphere.

The absorption frequencies and cross-sections of the Schumann–Runge bands are well known.[94,95] Thus, the troughs in the UVRR spectra caused by Schumann–Runge bands can serve as internal frequency standards for Raman spectral calibration. In fact, they could be used to independently determine the level of stray light present in the spectra.

Another possible application of the Schumann–Runge bands is to use them as very narrow frequency range absorption filters for suppressing Rayleigh lines in deep UV Raman spectroscopy. If the frequency of light used for UV Raman excitation coincides with that of a strong oxygen absorption band, the Rayleigh light scattering could be significantly attenuated, given the large oxygen absorption cross-sections, which are as high as ~10^{-19} cm^2 at wavelengths close to 180 nm.

To demonstrate the utility of our setup for fast transient measurements we studied the kinetics of apo-Mb folding. We utilized a T-jump from −3 to 10 °C in D_2O at pD ≈ 6. Between these temperatures apo-Mb undergoes refolding from a cold denaturated state to a more compact native state. Figure 13 shows the steady-state UVRR spectra of apo-Mb at −3 and 10 °C in D_2O. The amide backbone N-deuteration dramatically impacts the protein UVRR spectra, which is in D_2O dominated by an amide II' band that is almost a pure C–N stretch.[96] The hydrophobic core of apo-Mb is mostly α-helical.[97] Upon a temperature increase from −3 to 10 °C we observe that the intensity of the amide II' band decreases due to the α-helix fraction increase and the resulting hypochromism present in the intact α-helix folded conformations.

Figure 14A shows the transient difference spectra obtained by subtracting steady-state apo-Mb UVRR spectra at −3 °C from transient spectra measured at delays of 400 ns, 20 μs, and 300 μs subsequent to a T-jump from −3 to 10 °C. The major transient change observed is the amide II' intensity decrease observed in the steady-state measurement of Fig. 13. Transient difference spectra measured with delays shorter than 400 ns do not show significant spectral changes. Thus, the refolding process requires at least 400 ns to begin. Transient difference spectra at delays longer than 300 μs (not shown) are essentially identical to the steady-state difference spectrum, indicating that apo-Mb refolding is essentially complete within a few hundred microseconds.

The relaxation kinetics curve for apo-Mb shown in Fig. 14B fits well to a mono-exponential decay with a relaxation time of ~20 μs. This relaxation time is significantly longer than the typical ~200 ns delay times observed for short helical monomeric peptides.[51,98,99] This indicates an increase in constraints for α-helix folding in apo-Mb due to the tertiary interactions present for this protein. These kinetic results agree well with apo-Mb cold denaturation kinetic studies using methods such as fluorescence[100] and IR.[101]

CONCLUSION

We built a novel UV Raman spectrometer for steady-state and kinetic spectral measurements. Steady-state measurements can now be made with any excitation wavelengths between 193 and 270 nm, and with discrete

Nd:YAG harmonics and Raman shifted lines at discrete frequencies from the UV through the visible spectral region. High average powers together with low peak powers allow accumulation of high signal-to-noise UVRR spectra within short periods of time.

We constructed a novel high efficiency subtractive double spectrograph that is efficient in the deep UV region down to excitation wavelengths as short as 193 nm. We used two detectors to simultaneously measure high resolution spectra in the amide band region of proteins (~800–1800 cm^{-1}) and low resolution spectra in the water OH stretching band region (~2500–4000 cm^{-1}). This spectrometer can also be used with nanosecond Nd:YAG excitation for transient pump probe methods that permit T-jumps as well as electronic excitation by nanosecond pulses from the IR through the visible into the UV excitation region.

ACKNOWLEDGMENTS

The authors thank Bhavya Sharma, Konstantin Pimenov, Jonathan Scaffidi, and Zeeshan Ahmed for the help in preparing this manuscript. This work was supported by NIH grant 8RO1 EB002053021.

1. P. J. Hendra, *The Raman Spectroscopy of Polymers* (John Wiley and Sons, New York, 1993).
2. I. R. Lewis and H. G. M. E. Edwards, *Handbook of Raman Spectroscopy* (Marcel Dekker, New York, 2001).
3. J. M. Chalmers and G. Dent, *Instrumental Analysis with Raman Spectroscopy* (Royal Society of Chemistry, Cambridge, 1997).
4. Z. Huang, A. McWilliams, H. Lui, D. I. McLean, S. Lam, and H. Zeng, Int. J. Cancer **107,** 1047 (2003).
5. B. Schrader, B. Dippel, I. Erb, S. Keller, T. Lochte, H. Schulz, E. Tatsch, and S. Wessel, J. Mol. Struct. **480–481,** 21 (1999).
6. C. Krafft, Anal. Bioanal. Chem. **378,** 60 (2004).
7. N. S. Eikje, Y. Ozaki, K. Aizawa, and S. Arase, J. Biomed. Opt. **10,** 014013/1 (2005).
8. H. Schulz, M. Baranska, and R. Baranski, Biopolymers **77,** 212 (2005).
9. T. Hirschfeld and B. Chase, Appl. Spectrosc. **40,** 133 (1986).
10. D. A. Long, *The Raman Effect* (John Wiley and Sons, Chichester, 2002).
11. T. G. Spiro, Adv. Protein Chem. **37,** 111 (1985).
12. T. G. Spiro, G. Smulevich, and C. Su, Biochemistry **29,** 4497 (1990).
13. T. Kitagawa and T. Ogura, Adv. Spectrosc. (Chichester, United Kingdom) **21,** 139 (1993).
14. V. Palaniappan and D. F. Bocian, Biochemistry **33,** 14264 (1994).
15. K. Nakamoto, Coord. Chem. Rev. **226,** 153 (2002).
16. P. R. Carey, *Biochemical Applications of Raman and Resonance Raman Spectroscopies* (Academic Press, New York, 1982), Chap. 8, p. 100.
17. T. G. Spiro and C. A. Grygon, J. Mol. Struct. **173,** 79 (1988).
18. J. A. Sweeney and S. A. Asher, J. Phys. Chem. **94,** 4784 (1990).
19. P. J. Larkin, W. G. Gustafson, and S. A. Asher, J. Chem. Phys. **94,** 5324 (1991).
20. G. G. Kochendoerfer, S. Kaminaka, and R. A. Mathies, Biochemistry **36,** 13153 (1997).
21. L. Mayne and B. Hudson, J. Phys. Chem. **91,** 4438 (1987).
22. Z. Chi and S. A. Asher, J. Phys. Chem. B **102,** 9595 (1998).
23. V. W. Couling, P. Fischer, D. Klenerman, and W. Huber, Biophys. J. **75,** 1097 (1998).
24. L. Sokolov and I. Mukerji, J. Phys. Chem. B **104,** 10835 (2000).
25. Z. Q. Wen, S. A. Overman, P. Bondre, and G. J. Thomas, Jr., Biochemistry **40,** 449 (2001).
26. N. Haruta, M. Aki, S.-I. Ozaki, Y. Watanabe, and T. Kitagawa, Biochemistry **40,** 6956 (2001).
27. S. Hashimoto, M. Sasaki, H. Takeuchi, R. Needleman, and J. K. Lanyi, Biochemistry **41,** 6495 (2002).
28. A. Toyama, Y. Takahashi, and H. Takeuchi, Biochemistry **43,** 4670 (2004).
29. I. R. Rodriguez-Mendieta, G. R. Spence, C. Gell, S. E. Radford, and D. A. Smith, Biochemistry **44,** 3306 (2005).
30. R. A. Copeland and T. G. Spiro, Biochemistry **26,** 2134 (1987).
31. S. Song, S. A. Asher, S. Krimm, and J. Bandekar, J. Am. Chem. Soc. **110,** 8547 (1988).
32. S. A. Asher, Z. Chi, and P. Li, J. Raman Spectrosc. **29,** 927 (1998).
33. M. Xu, V. V. Ermolenkov, W. He, and I. K. Lednev, Abstracts of Papers, 229th ACS National Meeting (San Diego, CA, March 13–17, 2005**).**
34. S. A. Asher and C. R. Johnson, Science (Washington, D.C.) **225,** 311 (1984).
35. L. D. Ziegler and B. Hudson, J. Chem. Phys. **74,** 982 (1981).
36. S. A. Asher, C. R. Johnson, and J. Murtaugh, Rev. Sci. Instrum. **54,** 1657 (1983).
37. R. P. Rava and T. G. Spiro, J. Phys. Chem. **89,** 1856 (1985).
38. S. A. Asher, R. W. Bormett, X. G. Chen, D. H. Lemmon, N. Cho, P. Peterson, M. Arrigoni, L. Spinelli, and J. Cannon, Appl. Spectrosc. **47,** 628 (1993).
39. S. Hashimoto, T. Ikeda, H. Takeuchi, and I. Harada, Appl. Spectrosc. **47,** 1283 (1993).
40. M. P. Russell, S. Vohnik, and G. J. Thomas, Jr., Biophys. J. **68,** 1607 (1995).
41. V. Pajcini, C. H. Munro, R. W. Bormett, R. E. Witkowski, and S. A. Asher, Appl. Spectrosc. **51,** 81 (1997).
42. X. Zhao, C. Tengroth, R. Chen, W. R. Simpson, and T. G. Spiro, J. Raman Spectrosc. **30,** 773 (1999).
43. X. Zhao, R. Chen, C. Tengroth, and T. G. Spiro, Appl. Spectrosc. **53,** 1200 (1999).
44. M. C. Sparrow, J. F. Jackovitz, C. H. Munro, W. F. Hug, and S. A. Asher, Appl. Spectrosc. **55,** 66 (2001).
45. H. S. Sands, F. Demangeot, E. Bonera, S. Webster, R. Bennett, I. P. Hayward, F. Marchi, D. A. Smith, and D. N. Batchelder, J. Raman Spectrosc. **33,** 730 (2002).
46. I. K. Lednev, V. V. Ermolenkov, W. He, and M. Xu, Anal. Bioanal. Chem. **381,** 431 (2005).
47. Z. Chi, X. G. Chen, J. S. W. Holtz, and S. A. Asher, Biochemistry **37,** 2854 (1998).
48. S. Kaminaka, T. Ogura, and T. Kitagawa, J. Am. Chem. Soc. **112,** 23 (1990).
49. P. J. Reid, S. J. Doig, S. D. Wickham, and R. A. Mathies, J. Am. Chem. Soc. **115,** 4754 (1993).
50. V. Jayaraman, K. R. Rodgers, I. Mukerji, and T. G. Spiro, Science (Washington, D. C.) **269,** 1843 (1995).
51. I. K. Lednev, A. S. Karnoup, M. C. Sparrow, and S. A. Asher, J. Am. Chem. Soc. **121,** 8074 (1999).
52. I. K. Lednev, A. S. Karnoup, M. C. Sparrow, and S. A. Asher, J. Am. Chem. Soc. **123,** 2388 (2001).
53. X. Zhao, G. Balakrishnan, E. G. Moore, and T. G. Spiro, J. Raman Spectrosc. **31,** 349 (2000).
54. D. Wang, X. Zhao, and T. G. Spiro, J. Phys. Chem. A **104,** 4149 (2000).
55. N. Haruta and T. Kitagawa, Biochemistry **41,** 6595 (2002).
56. T. Kitagawa, N. Haruta, and Y. Mizutani, Biopolymers **61,** 207 (2002).
57. J. E. Kim, D. Pan, and R. A. Mathies, Biochemistry **42,** 5169 (2003).
58. J. Kneipp, G. Balakrishnan, and T. G. Spiro, J. Phys. Chem. B **108,** 15919 (2004).
59. S. A. Asher, Annu. Rev. Phys. Chem. **39,** 537 (1988).
60. R. W. Wood, Nature (London) **125,** 464 (1930).
61. M. Werth, Phys. Rev. **39,** 299 (1932).
62. J. Teraoka, P. A. Harmon, and S. A. Asher, J. Am. Chem. Soc. **112,** 2892 (1990).
63. C. M. Jones, V. L. Devito, P. A. Harmon, and S. A. Asher, Appl. Spectrosc. **41,** 1268 (1987).
64. C. Su, Y. Wang, and T. G. Spiro, J. Raman Spectrosc. **21,** 435 (1990).
65. J. S. W. Holtz, R. W. Bormett, Z. Chi, N. Cho, X. G. Chen, V. Pajcini, S. A. Asher, L. Spinelli, P. Owen, and M. Arrigoni, Appl. Spectrosc. **50,** 1459 (1996).
66. G. Balakrishnan, Y. Hu, S. B. Nielsen, and T. G. Spiro, Appl. Spectrosc. **59,** 776 (2005).
67. F. W. J. Teale, Biochim. Biophys. Acta **35,** 543 (1959).
68. F. Grum and G. W. Luckey, Appl. Opt. **7,** 2289 (1968).
69. W. Erb, Appl. Opt. **14,** 493 (1975).
70. E. R. Young, K. C. Clark, R. B. Bennett, and T. L. Houk, Appl. Opt. **19,** 3500 (1980).

71. V. Wilke and W. Schmidt, Appl. Phys. (Berlin) **16,** 151 (1978).
72. D. P. Gerrity, L. D. Ziegler, P. B. Kelly, R. A. Desiderio, and B. Hudson, J. Chem. Phys. **83,** 3209 (1985).
73. A. D. Papayannis, G. N. Tsikrikas, and A. A. Serafetinides, Appl. Phys. B **67,** 563 (1998).
74. S. Ameen, Rev. Sci. Instrum. **46,** 1209 (1975).
75. M. A. Donaldson, J. Sci. Instrum. **29,** 150 (1952).
76. V. Deckert, C. Fickert, D. Gernet, P. Vogt, T. Michelis, and W. Kiefer, Appl. Spectrosc. **49,** 253 (1995).
77. R. W. Bormett and S. A. Asher, Appl. Spectrosc. **48,** 1 (1994).
78. P. H. v. Cittert, Physica **3,** 181 (1923).
79. C. Leiss, Z. Phys. **77,** 412 (1932).
80. G. A. Boutry, *Instrumental Optics* (Interscience, New York, 1961), p. 532.
81. F. R. Lipsett, G. Oblinsky, and S. Johnson, Appl. Opt. **12,** 818 (1973).
82. R. E. Siemon, Appl. Opt. **13,** 697 (1974).
83. D. J. Dunstan and M. D. Frogley, Rev. Sci. Instrum. **73,** 3742 (2002).
84. R. Mathies, *Chemical and Biochemical Applications of Lasers*, C. B. Moor, Ed. (Academic Press, New York, 1979), vol. 4, p. 55.
85. B. R. Lewis, S. T. Gibson, L. W. Torop, and D. G. McCoy, GeoPhys. Res. Lett. **25,** 2457 (1998).
86. G. E. Walrafen, M. R. Fisher, M. S. Hokmabadi, and W. H. Yang, J. Chem. Phys. **85,** 6970 (1986).
87. N. Nishi, T. Nakabayashi, and K. Kosugi, J. Phys. Chem. A **103,** 10851 (1999).
88. X. G. Chen, D. H. Lemmon, R. W. Bormett, and S. A. Asher, Appl. Spectrosc. **47,** 248 (1993).
89. A. P. Demchenko, *Ultraviolet Spectroscopy of Proteins* (Spring-Verlag, New York, 1986).
90. S. A. Asher, A. V. Mikhonin, and S. Bykov, J. Am. Chem. Soc. **126,** 8433 (2004).
91. A. Ianoul, M. N. Boyden, and S. A. Asher, J. Am. Chem. Soc. **123,** 7433 (2001).
92. J. C. Austin, K. R. Rodgers, and T. G. Sprio, Methods Enzymol. **226,** 374 (1993).
93. S. A. Asher, A. Ianoul, G. Mix, M. N. Boyden, A. Karnoup, M. Diem, and R. Schweitzer-Stenner, J. Am. Chem. Soc. **123,** 11775 (2001).
94. K. Yoshino, D. E. Freeman, J. R. Esmond, and W. H. Parkinson, Planet. Space Sci. **31,** 339 (1983).
95. T. Matsui, A. S. C. Cheung, K. W. S. Leung, K. Yoshino, W. H. Parkinson, A. P. Thorne, J. E. Murray, K. Ito, and T. Imajo, J. Mol. Spectrosc. **219,** 45 (2003).
96. X. G. Chen, S. A. Asher, R. Schweitzer-Stenner, N. G. Mirkin, and S. Krimm, J. Am. Chem. Soc. **117,** 2884 (1995).
97. H. C. Shin, G. Merutka, J. P. Waltho, L. L. Tennant, H. J. Dyson, and P. E. Wright, Biochemistry **32,** 6356 (1993).
98. C.-Y. Huang, Z. Getahun, Y. Zhu, J. W. Klemke, W. F. DeGrado, and F. Gai, Proc. Natl. Acad. Sci. U.S.A. **99,** 2788 (2002).
99. T. Wang, Y. Zhu, Z. Getahun, D. Du, C.-Y. Huang, W. F. DeGrado, and F. Gai, J. Phys. Chem. B **108,** 15301 (2004).
100. R. M. Ballew, J. Sabelko, and M. Gruebele, Proc. Natl. Acad. Sci. U.S.A. **93,** 5759 (1996).
101. R. Gilmanshin, R. H. Callender, and R. B. Dyer, Nat. Struct. Biol. **5,** 363 (1998).